First steps towards creating multi-sensor DEMs using optimal weighting for change estimation and monitoring applications

Dimitrios BOLKAS[1,*], **Michael J. OLSEN**[2], **Erzhuo CHE**[2], and **Chase H. SIMPSON**[2]

[1] Department of Surveying Engineering, Pennsylvania State University, Wilkes-Barre, USA, (dxb80@psu.edu)

[2] School of Civil and Construction Engineering, Oregon State University, Corvallis, USA, (Michael.Olsen, erzhuo.che, chase.simpson)@oregonstate.edu

[*] *corresponding author*

Abstract

Digital elevation models (DEMs) are an important data product used in several geodetic applications to estimate changes associated with infrastructure management, rockfalls, landslides, soil migration, and beach loss and accretion. Current data acquisition methodologies often require integration of several point-cloud datasets from diverse platforms and sensors into a single DEM by leveraging the advantages of each dataset. However, optimizing the combination of these datasets is challenging because each dataset/sensor/platform has different measurement capabilities and acquisition methodologies, resulting in varying uncertainty structures. Further, the accuracy of individual point measurements can vary substantially within a single dataset. Rigorous uncertainty estimation is necessary to determine the optimal combination of measurements from these multi-sensor datasets to reliably estimate the elevation for each DEM cell. This paper uses rigorous error propagation and variance component estimation (VCE) to estimate the uncertainty throughout each point-cloud dataset. The updated uncertainty estimation then allows each dataset to be optimally weighted in the combined DEM. To demonstrate this methodology, we use datasets from terrestrial laser scanning (TLS), small uncrewed aircraft surveys (sUASs) with both imaging (photogrammetric) and Light Detection and Ranging (lidar) sensors to develop multi-epoch and multi-dataset DEMs for a test site at the Tumwata Village (Oregon, USA). The proposed method results in more robust DEMs with higher reliability, providing elevations with lower uncertainty compared to those developed without VCE. Finally, the elevations are accompanied by their own individual uncertainty estimations, which is useful to determine significant areas of change when analyzing multi-epoch datasets for change estimation or monitoring applications.

Keywords: Digital elevation model, multi-sensor fusion, laser scanning, UAS lidar, point cloud, variance component estimation.

Received: 9th December 2024. Revised: 24th February 2025. Accepted: 27th February 2025.

1 Introduction

One of the primary surveying products of mapping surveys is elevations in the form of Digital Elevation Models (DEMs). These elevations serve as the fundamental basis for several other engineering work such as landscape planning, earthwork volume calculations, stormwater drainage delineation, change analysis, and more. DEMs are often created to depict natural and man-made surface change estimations in applications such as soil migration, landslides, rockfalls, beach loss and accretion, and urban growth (e.g., Bolkas et al., 2016; Fernández et al., 2020; Bolkas et al., 2021; Bailey et al., 2022; Senogles et al., 2022; Li et al., 2024). Although DEMs offer a 2.5D representation, instead of a full 3D representation, they offer several advantages for spatial analysis including an easy-to-understand dataset format, ease of use, and efficient processing. Nowadays, DEMs can be derived from several platforms and methods including lidar and photogrammetric methods from terrestrial and aerial platforms. The availability of point cloud datasets from multiple sources in the same location is becoming more common, and their integration into a single DEM is often sought (Fernández et al., 2020; Okolie et al., 2022; Sudra et al., 2023). However, optimizing their

combination is challenging because of the diverse uncertainty structures and data acquisition methods associated with each dataset. A rigorous uncertainty estimation of each dataset is necessary to apply proper weights in the elevation estimation of each grid cell. This paper demonstrates the use of rigorous error propagation and variance component estimation (VCE) to derive reliable uncertainty estimates for each dataset. Then, using these updated uncertainty estimates, the datasets are combined to produce a single DEM. The advantage of this approach is that the optimal combination of the diverse datasets using rigorous statistical methods can lead to more accurate and consistent DEMs. In addition, through this approach, each grid cell of the DEM is accompanied by a rigorous uncertainty estimation, which then can be used to detect statistically significant changes in monitoring and other change estimation applications.

2 Methodology

Point clouds are generally scattered and unstructured datasets with highly variable point densities. An interpolation process is necessary to structure the multi-sensor and multi-platform data into a DEM for many applications. The optimized DEM in each epoch is estimated through a combination of multiple datasets acquired from different platforms. First, we perform error propagation for each dataset to derive uncertainty estimates individually. In the second step, the DEM surface estimation and VCE estimation occur simultaneously. Through the VCE the uncertainty of each dataset is updated, and a refined DEM surface estimation estimates the elevations for each cell. This process is depicted in the flowchart of Figure 1.

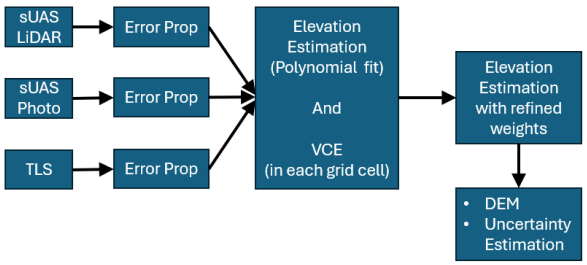

Figure 1. Flowchart outlining the proposed multiple sensor and platform DEM estimation.

A frequent challenge of DEM estimation using multiple datasets is dealing with vegetated areas. While lidar methods can penetrate vegetation to some degree, this generally is not the case for photogrammetric methods. In either case, the presence of vegetation produces increased uncertainty within both laser and photogrammetric point clouds. The site used in this study is free of vegetation in order to clearly demonstrate, develop, and evaluate the proposed algorithm. Hence, the algorithm currently assumes that any vegetation has been successfully filtered. Note that cofactor matrix notation is used for the TLS, sUAS photogrammetry, and sUAS lidar error propagation. The assumption made in these equations is that the "correct" covariance matrix is known only after the VCE occurs, and that the cofactor matrices are scaled using the estimated variance components.

2.1 TLS error propagation

The TLS error propagation is based on the methods found in (Lichti and Gordon 2004; Lichti, 2005; Hartzell et al., 2015) with the cofactor matrix given as:

$$\mathbf{Q}_{noise(TLS)} = \begin{bmatrix} q_\rho^2 + q_{BW_r}^2 & 0 & 0 \\ 0 & q_\theta^2 + q_{BW_a}^2 & 0 \\ 0 & 0 & q_\alpha^2 + q_{BW_a}^2 \end{bmatrix} \quad (1)$$

where, q_ρ is the ranging uncertainty, q_θ is the horizontal angular uncertainty, and q_α is the vertical angular uncertainty. q_{BW_a} is the angular uncertainty due to beam divergence, and q_{BW_r} is the range uncertainty due to the beam width and incidence angle. The angular and range uncertainty due to beam divergence are calculated based on the methods of Glennie (2007); Hartzell et al. (2015). The uncertainty of the TLS point cloud is derived through error propagation as follows:

$$\mathbf{Q}_{ENH(TLS)} = \mathbf{B}\mathbf{Q}_{noise(TLS)}\mathbf{B}^{\mathrm{T}} + \mathbf{Q}_{reg(TLS)} \quad (2)$$

where $\mathbf{Q}_{ENH(TLS)}$ is the 3×3 cofactor matrix for each point of the point cloud, $\mathbf{B}$ is the 3×3 matrix of partial derivatives of the laser scanner coordinates with respect to the laser scanner measurements, and $\mathbf{Q}_{reg(TLS)}$ is the 3×3 registration uncertainty for a scanner setup.

2.2 sUAS Photogrammetry error propagation

Obtaining uncertainty estimates from structure from motion (SfM) Multi-view Stereopsis (MVS) software can be challenging. Depending on the software used, the user can have no or limited information about the point cloud uncertainty. The uncertainties for the dense point cloud are interpolated from the sparse point cloud (tie point)

variance available in Metashape software (Agisoft LLC, 2019). To minimize interpolation errors, tie points are created to provide approximately 0.25 m average point spacing. This sampling provides sufficient detail for capturing uncertainty differences in the point cloud of this paper. Practitioners should consider an appropriate value for average point spacing based on the site characteristics and their proposed application. Ultimately, for each point of the sUAS photogrammetric point cloud we have a 3×3 cofactor matrix of the coordinate uncertainties:

$$\boldsymbol{Q}_{ENH(sUAS-photo)} = \begin{bmatrix} q^2_{E_{sUAS-photo}} & 0 & 0 \\ 0 & q^2_{N_{sUAS-photo}} & 0 \\ 0 & 0 & q^2_{H_{sUAS\_photo}} \end{bmatrix} \quad (3)$$

where $\boldsymbol{Q}_{ENH(sUAS-photo)}$ is the 3×3 cofactor matrix for each point of the point cloud, $q^2_{E_{sUAS-photo}}$, $q^2_{N_{sUAS-photo}}$, and $q^2_{H_{sUAS-photo}}$ are the variances for each coordinate.

2.3 sUAS lidar error propagation

One of the epochs used in this paper was augmented with a sUAS lidar dataset, offering a third platform of observation. The uncertainty is derived through error propagation of the system's error sources to the resulting point cloud. The sUAS lidar error propagation is based on the methods found in (Glennie, 2007; Bolkas et al., 2016), and the georeferencing approach of the DJI L1 sUAS lidar system (DJI 2024b; DJI 2024c). The covariance matrix is given as:

$$\mathbf{Q}_{sUAS(lidar)} = \begin{bmatrix} \mathbf{Q}_{GNSS} & \mathbf{0} & \mathbf{0} & \mathbf{0} \\ \mathbf{0} & \mathbf{Q}_{IMU} & \mathbf{0} & \mathbf{0} \\ \mathbf{0} & \mathbf{0} & \mathbf{Q}_{BS} & \mathbf{0} \\ \mathbf{0} & \mathbf{0} & \mathbf{0} & \mathbf{Q}_{scanner} \end{bmatrix} \quad (4)$$

where $\mathbf{Q}_{sUAS(lidar)}$ is a 12×12 cofactor matrix of the sUAS lidar system consisting of several 3×3 cofactor matrix including $\mathbf{Q}_{GNSS}$ for the GNSS measurements, $\mathbf{Q}_{IMU}$ 3×3 for the IMU angles, $\mathbf{Q}_{BS}$ for the boresight angles, and $\mathbf{Q}_{scanner}$ for the scanner unit. The uncertainty of the point cloud is derived through error propagation of the cofactor matrix in Eq. (4) using the sUAS lidar georeferencing equations as:

$$\mathbf{Q}_{ENH(sUAS-lidar)} = \mathbf{B}\mathbf{Q}_{sUAS(lidar)}\mathbf{B}^{\mathrm{T}} \quad (5)$$

where $\mathbf{Q}_{ENH(sUAS-lidar)}$ is the 3×3 cofactor matrix with the sUAS lidar point cloud coordinate uncertainties, and **B** is the 3×12 matrix of partial derivatives of the georeferencing equation with respect to the individual sUAS lidar uncertainty components and measurements.

2.4 sUAS lidar error propagation

Linear interpolation is used to derive the elevations of the DEM with the following equation:

$$l = p_{00} + p_{10}E + p_{01}N + p_{11}EN - H = 0 \quad (6)$$

where, $p_{00}, p_{10}, p_{01}, p_{11}$ are the linear interpolation coefficient parameters to be estimated, and E, N, H are the point cloud coordinates. For each grid cell, the points in its vicinity (radius equal to half the grid spacing) are selected and Eq. (6) is evaluated. Therefore, the matrix of observations of Eq. (6) is in the following form:

$$\mathbf{l} = \begin{bmatrix} \mathbf{l}_{TLS} \\ \mathbf{l}_{sUAS-photo} \\ \mathbf{l}_{sUAS-lidar} \end{bmatrix} \quad (7)$$

where, $\mathbf{l}_{TLS}$, $\mathbf{l}_{sUAS-photo}$, $\mathbf{l}_{sUAS-lidar}$ are the observations originating from each point cloud source. Their associated cofactor matrices are then given as:

$$\mathbf{Q}_l = \begin{bmatrix} \mathbf{Q}_{l_{TLS}} & \mathbf{0} & \mathbf{0} \\ \mathbf{0} & \mathbf{Q}_{l_{sUAS-photo}} & \mathbf{0} \\ \mathbf{0} & \mathbf{0} & \mathbf{Q}_{l_{sUAS-lidar}} \end{bmatrix} \quad (8)$$

where $\mathbf{Q}_l$ is the cofactor matrix of the observations / interpolation per grid cell, $\mathbf{Q}_{l_{TLS}}$, $\mathbf{Q}_{l_{sUAS-photo}}$, $\mathbf{Q}_{l_{sUAS-lidar}}$ are the cofactor matrices for each platform / dataset. These are derived through error propagation using Eq. (6) and the cofactor matrix of Eqs. (2), (3), and (5), which contain the coordinate variances. The size of these square matrices equals the number of points for each dataset for a specific grid cell. The Cofactor matrices are represented as a diagonal matrix for all three datasets. Cofactors were used because covariance information for the measurements was not available. Further, use of cofactors allowed for more efficient computations in developing this initial proof of concept. Lastly, covariance information can lead to sensitivity problems in the VCE if it cannot be accurately estimated. Future work will develop procedures to obtain and include covariance information by considering the spatial correlation of point cloud datasets.

It is assumed that any deviation from zero in Eq. (7) is due to the presence of measurement errors. Through VCE, the cofactor matrixes for each platform are scaled based on their local performance and contribution to the overall uncertainty. Therefore, Eq. (8) is modified as:

$$\mathbf{C}_l = \begin{bmatrix} \hat{\sigma}^2_{TLS}\mathbf{Q}_{l_{TLS}} & \mathbf{0} & \mathbf{0} \\ \mathbf{0} & \hat{\sigma}^2_{\substack{sUAS \\ -photo}}\mathbf{Q}_{l_{\substack{sUAS \\ -photo}}} & \mathbf{0} \\ \mathbf{0} & \mathbf{0} & \hat{\sigma}^2_{\substack{sUAS \\ -lidar}}\mathbf{Q}_{l_{\substack{sUAS \\ -lidar}}} \end{bmatrix} \quad (9)$$

where $\hat{\sigma}^2_{TLS}$, $\hat{\sigma}^2_{sUAS-photo}$, $\hat{\sigma}^2_{sUAS-lidar}$ are the variance component factors for each platform estimated through the VCE process. The VCE is performed using a simplified implementation of the best invariant quadratic unbiased estimates (BIQUE) approach (Koch 1986), which takes advantage of the structure of the cofactor matrices (Crocetto 2000) for disjunctive uncorrelated observation groups. This requires no correlation between dataset groups- i.e., the off-diagonal elements of matrix $\mathbf{Q}_l$ in Eq. (8) must be zero. This simplified approach is given as:

$$\hat{\sigma}_i^2 = \frac{\mathbf{I}_i^{\mathrm{T}}\mathbf{C}_{l_i}^{-1}\mathbf{Q}_{l_i}\mathbf{C}_{l_i}^{-1}\mathbf{I}_i}{\mathrm{trace}(\mathbf{R}_i\mathbf{Q}_{l_i}\mathbf{C}_{l_i}^{-1})} \quad (10)$$

where, the subscript *i* denotes the multi-platform dataset in each case (e.g., TLS, sUAS lidar, and sUAS photogrammetry), $\mathbf{c}_{l_i}$ for each dataset is derived as $\mathbf{c}_{l_{TLS}} = \hat{\sigma}^2_{TLS}\mathbf{Q}_{l_{TLS}}$, $\mathbf{c}_{l_{sUAS-photo}} = \hat{\sigma}^2_{sUAS-photo}\mathbf{Q}_{l_{sUAS-photo}}$, and $\mathbf{c}_{l_{sUAS-lidar}} = \hat{\sigma}^2_{sUAS-lidar}\mathbf{Q}_{l_{sUAS-lidar}}$. Matrix $\mathbf{R}$ is computed as:

$$\mathbf{R} = \mathbf{Q}_{\hat{\mathbf{v}}}\mathbf{C}_l^{-1} \quad (11)$$

where $\mathbf{Q}_{\hat{\mathbf{v}}}$ is the cofactor matrix of the adjustment residuals. The subscript *i* in Eq. (10) denotes the corresponding block-diagonal submatrix of matrix $\mathbf{R}$ for each dataset group. Having derived the variance component estimation, the linear interpolation and estimation steps are repeated to obtain a refined elevation and its associated uncertainty. In locations where only one dataset is present, the posterior variance is used to scale that dataset. When two or three datasets are present then VCE occurs to scale their cofactor matrices. The estimation takes place per grid cell; therefore, the variances are estimated based on the dataset characteristics in the vicinity of each grid cell. It is worth noting that modelling errors will also influence the interpolation in Eq. (6). For example, consider a case where the underlying surface consists of complex features (e.g., cliffs, walls, etc.). In such cases, linear interpolation would be insufficient to adequately capture these features. However, these issues are an inherent limitation in the ability of DEMs to represent complex surfaces. Although this model limitation would be expected to affect all datasets as well as the variance components in an absolute sense, it would likely have a minimal effect on their relative relationships. Therefore, the influence of these limitations in modelling techniques will be reflected in the elevation uncertainty because interpolation in complex areas will result in elevation estimations with higher uncertainty.

2.5 Multi-epoch comparison

Having constructed multi-platform / multi-sensor DEMs in each epoch, their elevation differences and change estimation can follow. We have constructed DEMs using the same grid pattern for consistency; therefore, elevation differences can be computed directly without further interpolation. The elevation difference between two corresponding grid cells is:

$$\Delta \mathrm{H}_{DEM_{i,i+1}} = \mathrm{H}_{DEM_{i+1}} - \mathrm{H}_{DEM_i} \quad (12)$$

where, $\Delta \mathrm{H}_{DEM_{i,i+1}}$ is the elevation difference between two DEMs observed in epochs *i* and *i*+1. $\mathrm{H}_{DEM_{i+1}}$ is the elevation at a grid cell in epoch *i*+1 and H_{DEM_i} is the elevation at a grid cell in epoch *i*. The uncertainty of the elevation difference is derived through error propagation:

$$\sigma_{\Delta \mathrm{H}_{DEM_{i,i+1}}} = \sqrt{\sigma^2_{\mathrm{H}_{DEM_{i+1}}} + \sigma^2_{\mathrm{H}_{DEM_i}}} \quad (13)$$

where, $\sigma_{\Delta \mathrm{H}_{DEM_{i,i+1}}}$ is the uncertainty in the DEM elevation difference between two epochs, $\sigma_{\mathrm{H}_{DEM_i}}$ and $\sigma_{\mathrm{H}_{DEM_{i+1}}}$ are the elevation uncertainties for each DEM, which are computed through error propagation (after VCE) in the linear interpolation step of Eq. (6). Significant changes are then estimated at the 95% confidence level as follows:

$$\left|\Delta \mathrm{H}_{DEM_{i,i+1}}\right| \geq t_{1-\alpha/2,df} \times \sigma_{\Delta \mathrm{H}_{DEM_{i,i+1}}} \quad (14)$$

where, $t_{1-\alpha/2,df}$ is the Student's critical value for α= 0.05 level (two tail test) and df are the degrees of freedom equal to the sum of points in the grid cells for the two DEMs. The elevation differences between two epochs ($\Delta \mathrm{H}_{DEM_{i,i+1}}$) are considered

significant when they exceed threshold $t_{0.025,df} \times \sigma_{\Delta H_{DEM_{i,i+1}}}$.

3 Research Site and Datasets

The research site is the Tumwata Village, formerly known as the Blue Heron Paper Mill, located at Willamette Falls, in Oregon City, Oregon. This historic site is currently under demolition in multiple phases as part of the effort to restore the ecological state of the site (https://www.tumwatavillage.org). The site has been routinely scanned to create a digital twin of the site to support a variety of applications, including preservation of important archaeological information, demolition and construction tracking, and floodplain analysis. Figure 2 depicts the site location and identifies the areas where multi-platform datasets were collected. Table 1 lists the areas and datasets that are available in each epoch and indicates which buildings have been demolished. Note that some of the buildings in areas 1 and 3 were demolished after the 2021 data collection.

Figure 2. The Tumwata Village in Oregon City, OR. The boxes outline the locations that are analyzed in this paper. The circles show the locations of the TLS setups capturing data within the four areas in 2022.

Table 1. Multi-platform data availability. P: sUAS Photogrammetry, L: sUAS lidar, T: terrestrial laser scanning.

Area	2021	2022	2023	Notes
1	P+T	P+L+T	P+T	Demolition in 2021
2	P+T	P+L+T	P+T	-
3	P+T	P+L+T	P+T	Demolition in 2021
4	P+T	P+L+T	P+T	-

Table 2 summarizes the average point spacing for each area, dataset, and epoch. Point spacing is generally between 1.0 cm to about 3.5 cm; however, the TLS dataset point spacing is more variable and depends on the number of setups and coverage in each area and epoch. For example, only a few setups were used in Areas 2 and 4 of the 2023 survey, resulting in data gaps and lowered average point spacing.

3.1 sUAS photogrammetry

Two sUAS photogrammetry systems were used in data collection. A DJI Phantom4 Pro was used in 2021, capturing approximately 1,200 photographs. A DJI Matrice with DJI P1 payload was deployed in 2022 and 2023 (DJI 2024a), resulting in about 2,000 and 1,200 photographs, respectively. Post-processed kinematic (PPK) GNSS data logged during the flights enabled precise estimation of the position of each frame to improve robustness in the photogrammetric process. Agisoft Metashape software was used to generate dense point cloud data through SfM and MVS processes following the guidelines in Over et al. (2021). The resulting ground sample density (GSD) for the point clouds in the three epochs were 4.2 cm, 2.5 cm, 3.0 cm for 2021, 2022, and 2023, respectively.

Table 2. Average point spacing for each area, dataset, and epoch. Units: cm.

Dataset	Epoch	Area 1	Area 2	Area 3	Area 4
TLS	2021	4.9	6.0	5.4	3.5
TLS	2022	1.6	3.3	2.1	2.8
TLS	2023	1.6	15.0	3.7	12.8
sUAS photo.	2021	3.7	4.1	3.2	4.3
sUAS photo.	2022	2.2	2.4	2.4	2.4
sUAS photo.	2023	2.8	3.0	2.8	3.0
sUAS lidar	2022	3.5	1.0	2.5	2.2

3.2 sUAS lidar

The sUAS lidar data were collected using a DJI Matrice 300 carrying the DJI L1 sensor (DJI 2024b; DJI 2024c) in the 2022 campaign. The sUAS system is quoted as being capable of achieving a horizontal accuracy of 10 cm at 50 m and vertical accuracy of 5 cm at 50 m, both at the 1-σ level. The specifications state that the lidar ranging accuracy is 3 cm at 100 m and the angular accuracy is 0.05º (1-σ) with beam divergence of 0.28º (vertical) and 0.03º (horizontal) (Livox 2024). After post-processing the IMU angular measurement accuracies are quoted as 0.15º (1-σ) for yaw, and 0.025º (1-σ) for pitch and roll. The pulse rate is

240,000 points / second for single return, 480,000 points / for dual return and 720,000 points/ second for triple return. Data were collected at an altitude of 60 m using the dual return option and maintaining an overlap of about 50% between adjacent swaths.

3.3 Terrestrial laser scanning

TLS data were collected using a Leica Scan Station P50 (Leica Geosystems, 2024) with a resolution of 3 mm at 10 m. The scanner has a range accuracy of 1.2 mm + 10 ppm (1-σ), horizontal and vertical angular accuracy of 8″, and beam divergence of 0.23 mrad (full width at half maximum). Scan registration was performed using a combination of cloud-to-cloud surface matching and targets distributed across the scene. Several target coordinates were obtained from a network adjustment of a control survey combining static GNSS baseline surveys on ground control points with total station traverse measurements. The registration uncertainty was estimated using the target registration residuals and typically within 5 mm.

4 Results

4.1 VCE Results

Table 3 provides the elevation uncertainty for each dataset, area, and epoch. Only elevation uncertainty is shown for simplicity and because it is the primary component of a DEM.

Table 3. Median elevation uncertainty for each area, dataset, and epoch. Units: mm.

Dataset	Epoch	Area 1	Area 2	Area 3	Area 4
TLS	2021	7.3	4.5	3.3	3.4
TLS	2022	2.6	4.9	3.0	2.5
TLS	2023	2.7	22.5	20.4	2.7
sUAS photo.	2021	50.2	58.3	94.6	70.2
sUAS photo.	2022	5.8	32.4	14.2	6.4
sUAS photo.	2023	5.2	18.3	5.7	5.6
sUAS lidar	2022	59.4	45.6	61.3	59.0

The TLS survey, as expected, has the lowest propagated uncertainty apart from a couple of areas that only contain sparse data (Table 2) from long-range scans observed at high incidence angles. The propagated elevation uncertainty of the sUAS lidar survey is consistent with the manufacturer specifications. The sUAS photogrammetric survey shows more variable results due to the different aircrafts and sensors that were used for each epoch. The data obtained from the DJI Phantom 4 Pro platform used in 2021 show substantially higher uncertainty compared with the DJI Matrice used in 2022 and 2023. Using Eq. (6) and the cofactor matrices of Eqs. (2), (3), and (5) the vertical and horizontal coordinate uncertainties are propagated to each interpolated elevation. Through VCE the covariance matrix of each dataset is then scaled. Table 4 shows the median scale estimated for each area, dataset, and epoch. Note unitless scales (standard deviation) are provided for the covariance matrix in Eq. (9), which do not directly correspond to those in Table 3, because both the elevation and horizontal uncertainty contribute to interpolation error.

Table 4. Median VCE results for each area, dataset, and epoch. The standard deviation is provided instead of the variance to assist with interpretation. Units: unitless.

Dataset	Epoch	Area 1	Area 2	Area 3	Area 4
TLS	2021	0.25	0.17	0.16	0.41
TLS	2022	0.41	0.21	0.95	0.80
TLS	2023	0.96	0.17	0.45	0.71
sUAS photo.	2021	0.20	0.10	0.13	0.11
sUAS photo.	2022	1.92	0.16	0.80	0.62
sUAS photo.	2023	0.69	0.14	0.45	0.55
sUAS lidar	2022	0.44	0.51	1.71	0.48

Figure 3 provides a visual representation of the scales for each grid cell to assist with interpretation. The uncertainty appears to be overestimated for almost all datasets, with a couple of exceptions. A few sections have been highlighted to guide the discussion. For instance, in Figure 3a, the sUAS photogrammetric dataset results in higher scales, indicative of the overall higher reconstruction uncertainty. The TLS dataset contains high scales in an area containing a pile of logs. In Figure 3b an occlusion with the sUAS photogrammetric dataset leads to higher scales due to increased uncertainty. In Figure 3d for the sUAS photogrammetric dataset, an area of poor image alignment resulted in a small offset compared to the TLS dataset. Finally, the sUAS lidar dataset demonstrates consistent scales (and uncertainty), compared to the other two datasets. These results demonstrate the benefit of conducting surveys with multiple sensors, as a more complex and thorough statistical analysis can take place to evaluate and refine the uncertainties of each

dataset. Essentially, through the VCE approach, each dataset is checking the other for their consistency, which in turn allows identification of uncertainty deviations to update the covariance matrices. Furthermore, the results presented in Table 4 and Figure 3 demonstrate how point cloud uncertainty can be variable and primarily depends on the (1) sensor used, (2) the data collection strategy, (3) processing methods, and (4) the encountered surface characteristics.

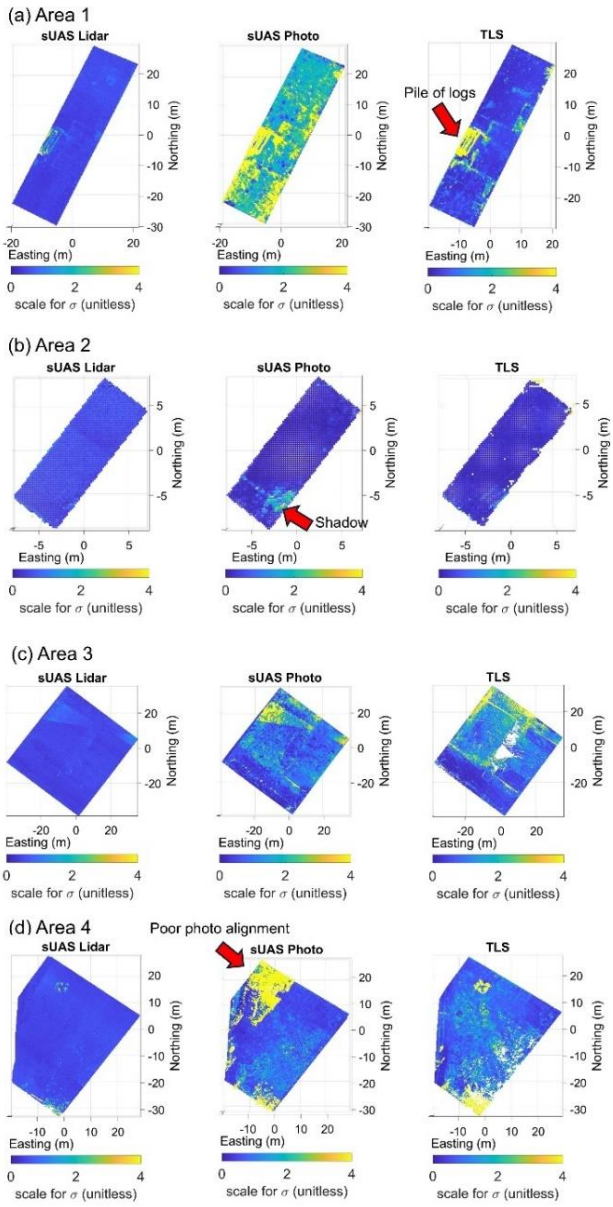

Figure 3. VCE results for each area and dataset in 2022; (a) Area 1; (b) Area 2; (c) Area 3; (d) Area 4.

The VCE algorithm is implemented through a polynomial fit approach and thus can be influenced by the dataset containing the largest number of points. This becomes relevant in vegetated areas. If there are considerably more ground points (from lidar) than non-ground points (from photogrammetry) then the polynomial fit will favor the largest dataset and the variance of the non-ground points, which are influenced by vegetation, will be scaled as having higher error. However, in cases where the non-ground points outnumber the ground points, the algorithm may consider that the correct fit is dictated by the non-ground points and the ground point variances will be scaled as having higher error. To resolve the conflict higher weights can be placed on the ground points (if the information exists through classification) and they can be constrained in each iteration to avoid the influence of non-ground points. Note that this was not implemented and tested here but is being considered in future work. Additional investigation and specific tests are needed to provide a thorough analysis and reach safer conclusions that are beyond the scope of this study.

4.2 DEM and Uncertainty Estimation

After the refinement of the covariance matrices, the DEM is created through linear interpolation using Eq. (6). In this section we provide three weighting schemes in the creation of the multi-sensor DEM, presented in increasing rigor. The first weighting scheme assumes that no information about the dataset uncertainty (and hence their weights) is available. Therefore, all datasets are given the same weight. This approach is most common in practice as most software packages do not provide users with the ability to weigh points in the modeling process. The second scheme considers the uncertainty from error propagation using the manufacturer specifications but without the application of VCE. The third scenario uses the refined uncertainty estimates [covariance matrix in Eq. (9)] using the scales that were presented in the previous section. This last scenario leverages the existence of multiple datasets in the same location to refine their uncertainty estimates (and associated weights). Table 5 shows the median DEM elevation uncertainty for the three difference weighting schemes.

Table 5. Median DEM elevation uncertainty for three different weighting schemes in 2022.

Dataset	Area 1	Area 2	Area 3	Area 4
Equal weights	0.8 mm	1.4 mm	1.4 mm	1.5 mm
Weights error prop.	0.2 mm	0.7 mm	0.5 mm	0.3 mm
Weights VCE	0.1 mm	0.2 mm	0.4 mm	0.2 mm

As expected, the equal weighting scheme has the highest uncertainties because data points with high uncertainty are allowed to contribute equally with low uncertainty data points. The median uncertainty is at the level of 0.8 mm to 1.5 mm in the four areas that are examined here. The median uncertainties derived in the second scenario when the weights are estimated through error propagation are at the level of 0.2 mm to 0.7 mm for the four areas. When the weights are estimated through the proposed VCE scheme, the median elevation uncertainties are at the level of 0.1 mm to 0.4 mm. Figure 4 visually depicts the DEM elevation uncertainty for each weighting scheme in Area 4.

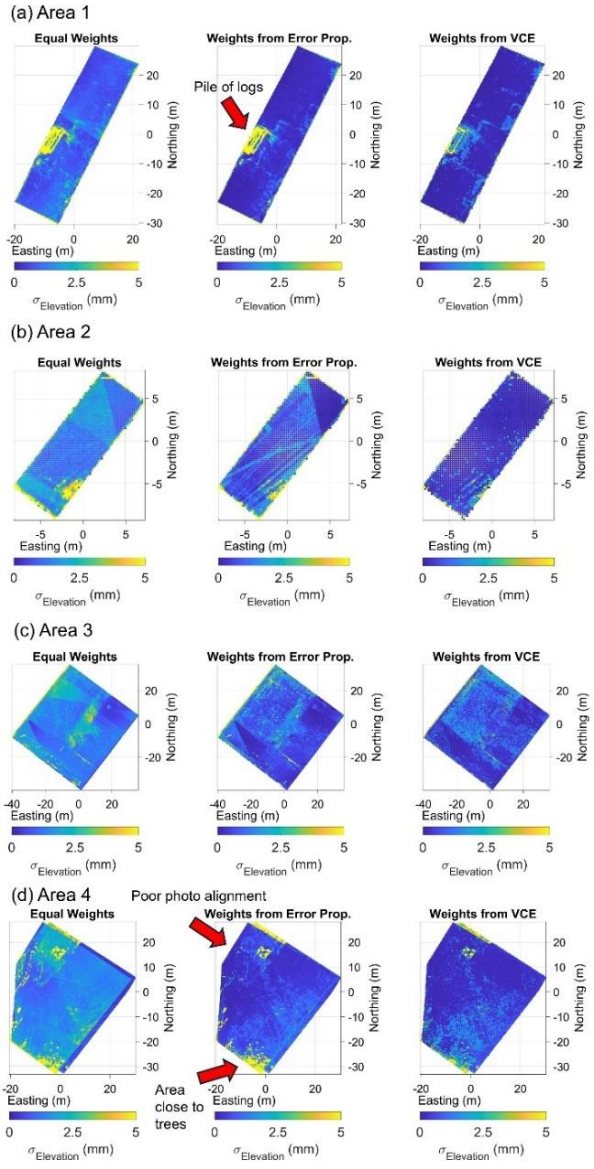

Figure 4. Multi-sensor DEM uncertainty for each area in 2022; (a) Area 1; (b) Area 2; (c) Area 3; (d) Area 4. Each figure set shows three combination scenarios (1) equal weights, (2) weights from error propagation, and (3) weights from VCE.

It is evident that when improper weights are used, the combined DEM will have high uncertainty as shown in the case of equal weights. However, we also observe that in the case of error propagation there is always a certain level of overestimation / underestimation of uncertainty for each dataset, which cannot lead to their optimal (in terms of uncertainty) DEM combination. An optimal multi-sensor DEM estimation is possible when the dataset uncertainty is refined through a VCE process as demonstrated in this paper. Furthermore, an important outcome of the VCE multi-sensor combination is that areas of higher error in one of the three datasets are checked by the other datasets; therefore, their contribution is limited when using the refined weights. For instance, this happens in Area 4 close to trees that led to higher uncertainty and the poor image alignment. The level of improvement will vary based on the mismatch of each dataset in each area and the level of deviation from an optimal weighting scheme among the three datasets. The results in this section demonstrate the ability of the VCE approach to scale the original uncertainty of each dataset and optimally weight them to derive enhanced multi-sensor DEMs.

4.3 Change estimation

In the next step the multi-sensor DEMs are utilized to create multi-epoch comparisons and detect any changes between the 2021 and 2022 surveys and between 2022 and 2023 surveys in the four areas. Table 6 shows the percentage of cells that were found to significantly change between two epochs (between surveys 1 and 2 and between surveys 2 and 3). In general, a high number of cells were found to change, with percentages ranging from 88.3% to 100%. Note that this is an active construction site, undergoing active demolition; hence, significant changes are expected for much of the site. For instance, within Areas 1 and 3 the buildings that were present in epoch 1 were demolished in epoch 2. Furthermore, surface activity such as moving vehicles, construction workers moving, and natural environment changes (e.g., due to rain) also contribute. Comparing the three weighting schemes we notice differences at the level of 1-5% for the error propagation weights and VCE weights. The maximum difference between the two approaches was found in Area 3 (epochs 2 vs 3).

Table 6. Percentage of cells that were detected to significantly change between surveys 1 and 2 and 2 and 3. Total cell counts are: Area 1, 24974; Area 2 2695; Area 3, 71649; Area 4; 42246.

Dataset	Epoch	Area 1	Area 2	Area 3	Area 4
Equal weights	1 vs 2	100%	89.9%	93.6%	88.3%
Weights error prop.	1 vs 2	100%	93.2%	93.9%	92.8%
Weights VCE	1 vs 2	100%	95.5%	94.4%	93.2%
Equal weights	2 vs 3	94.7%	97.0%	91.8%	91.9%
Weights error prop.	2 vs 3	95.0%	97.0%	95.0%	96.0%
Weights VCE	2 vs 3	93.7%	98.5%	90.4%	96.7%

Figure 5 shows the number of cells detected as significantly changed, and Figure 6 shows the DEM differences between the two epochs. To emphasize lower values, the colorbar is limited to ± 20 mm. It is worth noting that only a few grid cells have differences less than ± 20 mm, which highlights the level of anthropogenic and construction activity at this site. We also notice that the biggest changes between the three weighting schemes are located near the center of the area, where through VCE weighting we observe that the DEM elevations differences tend to be at the level of ± 2-3 mm compared with ± 5 mm when estimated using the error propagation weights.

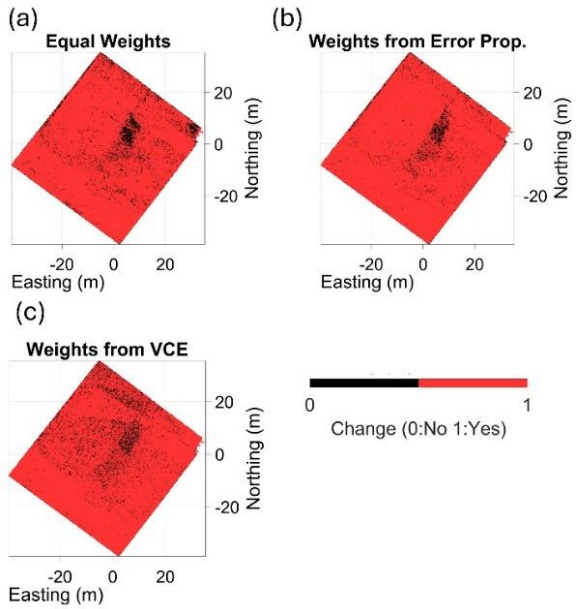

Figure 5. Significant changes of Area 3, epoch 2 vs 3; (a) equal weights, (b) weights from error propagation; (c) weights from VCE. 0 means no significant change and 1 means significant change at the 95% confidence level.

5 Conclusions

DEMs are an important mapping product for a wide range of applications including monitoring and change detection. The availability of multi-sensor datasets allows one to create optimized multi-sensor and multi-platform DEMs, which can leverage the benefits of each sensor and platform. However, their combination can be challenging due to the variable uncertainties inherent to each dataset. This paper implements rigorous error propagation and a VCE approach to obtain refined variances for each dataset and therefore construct DEMs through an optimal weighting of each point cloud dataset. The results of this paper demonstrated how the VCE effectively managed to scale each grid cell uniquely based on the local data uncertainty. The three weighting schemes tested here demonstrate that improper weighting between the dataset can lead to DEMs with higher uncertainty, and that, in all cases, the combination with weights derived from VCE presented the lowest uncertainty. This was also demonstrated in the epoch-to-epoch comparisons, where the VCE weights were able to provide an improved estimation of the differences between the two DEMs. Future work will focus on testing the algorithm in more sites and types of terrain to further validate the algorithm and expand its capabilities.

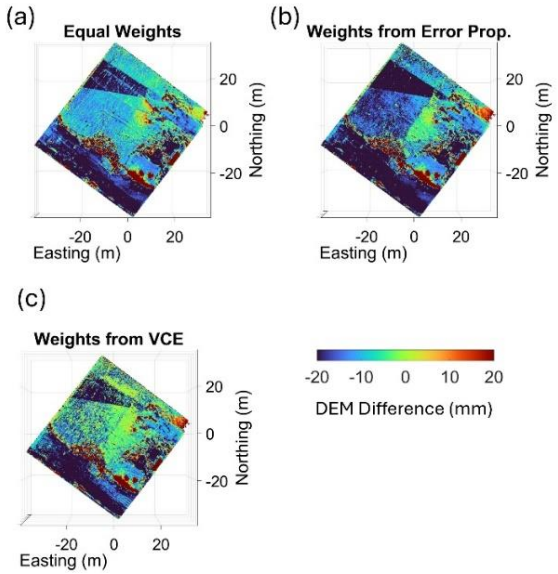

Figure 6. DEM differences between epochs 2 vs 3 for Area 3; (a) equal weights, (b) weights from error propagation; (c) weights from VCE.

Acknowledgements

Funding supporting the data collection was provided by the National Science Foundation (NSF) under awards 1937070 and 2228113, and the

National Geospatial Intelligence Agency GeoEscon program. Approved for public release, NGA-U-2024-09711. We gratefully acknowledge the support of Leica Geosystems and Kuker Ranken in providing equipment and software for this study. The Confederated Tribes of the Grand Ronde Community of Oregon graciously provided access to the Tumwata Village site where the data were collected. Lastly, the authors acknowledge the efforts of the many Oregon State University Geomatics graduate students who assisted with the data collection.

References

Agisoft LLC. (2019). Forum, Topic: Point Cloud Variance; https://www.agisoft.com/forum/index.php?topic=10805.0 [Accessed 4 October 2024]

Bailey, G., Li, Y., McKinney, N., Yoder, D., Wright, W., Washington-Allen, R., (2022). Las2DoD: Change detection based on digital elevation models derived from dense point clouds with spatially varied uncertainty. *Remote Sensing*, 14(7), 1537.

Bolkas, D., Fotopoulos, G. Glennie, C., (2016). On the impact of a refined stochastic model for airborne LiDAR measurements. *Journal of Applied Geodesy*, 10(3), 185-196.

Bolkas, D., Walton, G., Kromer, R., Sichler, T., (2021). Registration of multi-platform point clouds using edge detection for rockfall monitoring. *ISPRS Journal of Photogrammetry and Remote Sensing*, 175, 366-385.

Crocetto, N., Gatti, M., Russo, P. (2000). Simplified formulae for the BIQUE estimation of variance components in disjunctive observation groups. *Journal of Geodesy*, 74, 447-457.

DJI. (2024a). Zenmuse PI. https://www.dji.com/zenmuse-p1?site=brandsiteandfrom=nav. [Accessed 7 November 2024]

DJI. (2024b). Zenmuse L1. https://www.dji.com/zenmuse-l1/specs. [Accessed 7 November 2024]

DJI. (2024c). Zenmuse L1 user manual. https://dl.djicdn.com/downloads/Zenmuse_L1/20220119UM/Zenmuse_L1%20_User%20Manual_EN_v1.2-1.pdf. [Accessed 7 November 2024]

Glennie, C., (2007). Rigorous 3D error analysis of kinematic scanning LIDAR systems. *Journal of Applied Geodesy*, 1, 147-157.

Hartzell, P.J., Gadomski, P.J., Glennie, C.L., Finnegan, D.C. and Deems, J.S., (2015). Rigorous error propagation for terrestrial laser scanning with application to snow volume uncertainty. *Journal of Glaciology*, 61(230), 1147-1158.

Fernández, T., Pérez-García, J.L., Gómez-López, J.M., Cardenal, J., Calero, J., Sánchez-Gómez, M., Delgado, J. and Tovar-Pescador, J., (2020). Multitemporal analysis of gully erosion in olive groves by means of digital elevation models obtained with aerial photogrammetric and LiDAR data. *ISPRS International Journal of Geo-Information*, 9(4), 260.

Koch, K. R. (1986). Maximum likelihood estimate of variance components. *Bulletin gœodésique*, 60, 329-338.

Leica Geosystems (2024). Leica ScanStation P50 – Long Range 3D Terrestrial Laser Scanner. Leica Geosystems. https://leica-geosystems.com/en-us/products/laser-scanners/scanners/leica-scanstation-p50 [Accessed 7 November 2024]

Li, P., Li, D., Hu, J., Fassnacht, F.E., Latifi, H., Yao, W., Gao, J., Chan, F.K.S., Dang, T., Tang, F., (2024). Improving the application of UAV-LiDAR for erosion monitoring through accounting for uncertainty in DEM of difference. *Catena*, 234, 107534.

Lichti, D.D. Gordon, S.J., (2004). Error propagation in directly georeferenced terrestrial laser scanner point clouds for cultural heritage recording. *Proc. of FIG Working Week*, Athens, Greece, May, 22-27.

Lichti, D.D., Gordon, S.J., Tipdecho, T., (2005). Error models and propagation in directly georeferenced terrestrial laser scanner networks. *Journal of surveying engineering*, 131(4), 135-142.

Livox. (2024). Avia Specs. Livox. https://www.livoxtech.com/avia/specs [Accessed 8 November 2024]

Okolie, C.J. and Smit, J.L., (2022). A systematic review and meta-analysis of Digital elevation model (DEM) fusion: Pre-processing, methods and applications. *ISPRS Journal of Photogrammetry and Remote Sensing*, 188, 1-29.

Over, J. S. R., Ritchie, A. C., Kranenburg, C. J., Brown, J. A., Buscombe, D. D., Noble, T., Sherwood, C.R., Warrick, J.A and Wernette, P. A. (2021). Processing coastal imagery with Agisoft Metashape Professional Edition, version 1.6—Structure from motion workflow documentation (No. 2021-1039). *US Geological Survey*. https://pubs.usgs.gov/of/2021/1039/ofr20211039.pdf [Accessed 7 November 2024]

Senogles, A., Olsen, M. J., Leshchinsky, B. (2022). SlideSim: 3D landslide displacement monitoring through a physics-based simulation approach to self-supervised learning. *Remote Sensing*, 14(11), 2644.

Sudra, P., Demarchi, L., Wierzbicki, G., Chormański, J., (2023). A comparative Assessment of Multi-source Generation of Digital Elevation Models for Fluvial landscapes characterization and monitoring. *Remote Sensing*, 15(7), 1949.